JOURNAL OF GEOPHYSICAL RESEARCH, VOL. 113, B11412, doi:10.1029/2008JB005588, 2008

Experimental measurements of permeability evolution during triaxial compression of initially intact crystalline rocks and implications for fluid flow in fault zones

T. M. Mitchell[1,2] and D. R. Faulkner[1]

Received 13 January 2008; revised 25 June 2008; accepted 7 August 2008; published 26 November 2008.

[1] Detailed experimental studies of the development of permeability of crustal rock during deformation are essential in helping to understand fault mechanics and constrain larger-scale models that predict bulk fluid flow within the crust. Permeability is particularly enhanced in the damage zone of faults, where microfracture damage accumulates under stress less than that required for macroscopic failure. Experiments performed in the prefailure region can provide data directly applicable to these zones of microfracture damage surrounding faults. The strength, permeability, and pore fluid volume evolution of initially intact crystalline rocks (Cerro Cristales granodiorite and Westerly granite) under increasing differential load leading to macroscopic failure has been determined at water pore pressures of 50 MPa and varying effective pressures from 10 to 50 MPa. Permeability is seen to increase by up to, and over, 2 orders of magnitude prior to macroscopic failure, with the greatest increase seen at lowest effective pressures. Postfailure permeability is shown to be over 3 orders of magnitude higher than initial intact permeabilities and approaches the lower limit of predicted in situ bulk crustal permeabilities. Increasing amplitude cyclic loading tests show permeability-stress hysteresis, with high permeabilities maintained as differential stress is reduced and the greatest permeability increases are seen between 90 and 99% of the failure stress. Prefailure permeabilities are nearly 7 to 9 orders of magnitude lower than that predicted by some high-pressure diffusive models suggesting that if these models are correct, microfracture matrix flow cannot dominate, and that bulk fluid flow must be dominated by larger-scale structures such as macrofractures. We present a model, based on our data, in which the permeability of a highly stressed fault tip process zone in low-permeability crystalline rocks increases by more than 2 orders of magnitude. Stress reduction related to the onward migration of the fault tip close damage zone cracks, while some permeability is maintained due to hysteresis from permanent microfracture damage.

Citation: Mitchell, T. M., and D. R. Faulkner (2008), Experimental measurements of permeability evolution during triaxial compression of initially intact crystalline rocks and implications for fluid flow in fault zones, *J. Geophys. Res.*, *113*, B11412, doi:10.1029/2008JB005588.

1. Introduction

[2] Experimental constraints on the evolution of permeability of crustal rock with deformation are fundamental in helping to understand bulk fluid flow within the crust. Models predicting crustal fluid flow are important for a variety of reasons; for example earthquake models invoking fluid triggering [e.g., *Nur and Booker*, 1972; *Sibson*, 1974; *Miller et al.*, 2004], predicting crustal strength [*Townend and Zoback*, 2000] or modeling flow surrounding deep waste repositories. Crustal fluid flow is controlled by both the bulk transport properties of rocks as well as heterogeneities such as faults. Fracture damage on all scales affects the permeability of rock and understanding these variations is important as it gives an invaluable insight into the pathways and barriers for fluid flow [*Knipe*, 1992; *Caine et al.*, 1996; *Shipton et al.*, 2002].

[3] Fluid flow around fault zones is dictated by both the properties of the fault core and the surrounding fracture damage zone. Low permeability fault core material can act a fluid barrier and trap fluids within faults zones, and this can lead to the development of pressures in excess of hydrostatic that commonly approach lithostatic [*Byerlee*, 1990]. High-pressure fluid sealing and weakening models [*Blanpied et al.*, 1992; *Rice*, 1992; *Faulkner and Rutter*, 2001] rely on interconnected fault networks within core and damage zones. The fluid flow properties of the fracture damage zone surrounding faults are relatively poorly constrained. Damage

[1]Rock Deformation Laboratory, Department of Earth and Ocean Sciences, University of Liverpool, Liverpool, UK.
[2]Now at Graduate School of Science, Department of Earth and Planetary Systems Science, Hiroshima, Japan.

0148-0227/08/2008JB005588$09.00

exists on all scales but is often considered on two primary scales for convenience; macroscopic fracturing, observable at the field scale, and microfracture damage on the grain scale. Macroscopic damage such as shear fractures and joints are often referred to as intermediate scale damage, as with increasing displacement such shear fractures can develop into large-scale fault zones.

[4] It has been demonstrated from experiments and modeling that faults and fractures in brittle rock are formed through the interaction and coalescence of many tensile microcracks [*Lockner et al.*, 1991; *Lockner et al.*, 1992; *Reches and Lockner*, 1994; *Healy et al.*, 2006]. This suggests that when differential stress is applied to intact rock samples, microfracture damage accumulates as the rock approaches failure, and the resultant progressive dilatancy will have a direct effect on both porosity and permeability. Indeed, various mechanical models suggest intense zones of microfracturing in the "process zone" surrounding highly stressed fault tips (e.g., *Scholz et al.* [1993] and see also review by *Dresen and Guéguen* [2004]) which decrease in density with distance from the fault and increase in size with increased fault length. Field studies of microfracture damage surrounding natural faults support these models in that they show a log linear decrease of microfracture density with distance from the fault [e.g., *Anders and Wiltschko*, 1994; *Vermilye and Scholz*, 1998; *Wilson et al.*, 2003; *Faulkner et al.*, 2006], although this pattern could also be explained by other mechanical processes operative during accumulating slip displacement. For example, wear models [e.g., *Chester and Chester*, 2000] suggest continued slip on preexisting fault surfaces introduces cumulative damage into the surrounding rock. More recently, work has focused on fracture damage that is suggested to be created by the elastic strain energy released during dynamic rupture in the form of dynamic slip pulses. Modeling suggests that these pulses can cause considerable off-fault damage in the form of general off-fault secondary failure or pulverized rock at shallower levels [*Rice et al.*, 2005; *Dor et al.*, 2006].

[5] Whatever underlying processes are dominant, a key factor is that microfracture damage surrounding fault zones is manifest and varies significantly and hence will have a direct effect on permeability surrounding faults. Even macroscopic fractures surrounding larger faults will themselves have associated microfracture damage zones. This highlights the importance of understanding the relationship between progressive fracture damage and permeability.

[6] It is the aim of this paper to attempt to provide quantitative data from the laboratory to constrain the fluid flow properties of the microfracture component of the damage zone. In nature, the damage zone rocks contain microfractures that vary as a function of distance from the fault core, and they will have experienced differential stresses that were less than, but some proportion of, the failure stress. As such, permeability data from progressively loaded, initially intact laboratory samples, in the prefailure region should provide useful insights into fluid flow properties of various parts of the damage zone. As differential stress increases and microfractures accumulate as samples reach higher proportions of the failure stress, the fluid flow data should be more applicable to those parts of natural fault damage zones that are close to the fault core.

[7] Experimental determination of permeability evolution of crystalline rocks during progressive deformation has received remarkably little attention in the literature. Various studies have examined the pre and postfailure permeability evolution of porous clastic rocks (sandstones with initial porosities ranging from 4.5 to >14%) under increasing differential stress [*Zhu and Wong*, 1997; *Keaney et al.*, 1998; *Heiland*, 2003; *Zhang et al.*, 2007]. *Uehara and Shimamoto* [2004] reported results of permeability measurements of fault gouge and tonalitic cataclasite from the fault zone of the Median Tectonic Line, Ohshika, central Japan, carried out during progressive axial deformation under triaxial conditions. However, few data exist for intact crystalline rocks such as granites which can have porosities lower than 1%. *Zoback and Byerlee* [1975] produced one of the only studies on the permeability evolution of granite under increasing differential stress. They determined permeability under stepwise increasing axial stress at effective confining pressures of 39 and 14 MPa. Rock specimens were loaded up to a maximum differential stress of only ~80% of their peak strength and showed increases in permeability of around 300%.

[8] In most previous work [e.g., *Zoback and Byerlee*, 1975; *Zhu et al.*, 1997; *Keaney et al.*, 1998] the pulse transient technique for permeability measurement was used [*Brace et al.*, 1968; *Sanyal et al.*, 1972]. This requires the axial load actuator to be stopped while permeability is measured. This may introduce the problem of creep, due to the fact that once dilatancy has initiated, rocks exhibit stable crack growth [*Atkinson and Meredith*, 1987] while under load. As a result of the actuator being stopped and hence fixed, axial stress relaxation can lead to increasing lateral strain that influences permeability. *Keaney et al.* [1998] suggested stopping the actuator movement results in a nonsteady state permeable microstructure in the rock, especially in the dilatant deformation phase. In these studies, different techniques were used to reduce the effect of creep on permeability measurements. For example, *Keaney et al.* [1998] reduced the axial load during the permeability measurements during a standardized procedure in order to achieve steady state condition. *Heiland* [2003] tried to suppress lateral deformation while the actuator was stopped by controlling the lateral strain by varying the confining pressure.

[9] In this paper we describe the results of conventional triaxial deformation experiments ($\sigma_1 > \sigma_2 = \sigma_3$) on low-porosity crystalline rocks where permeability and pore volume were continuously monitored up to the failure of the specimens. Experiments were conducted at effective pressures ranging from 10 to 50 MPa. First, we outline the experimental techniques used to collect the data. Then, the variations in permeability of initially intact crystalline rock right up to macroscopic failure of samples are presented. The results from increasing amplitude cyclic loading tests where cumulative damage and permeability hysteresis was monitored is then shown. Finally, the experimental results are used as a framework to assess the permeability structure surrounding fractures and faults and the implications for fault zone hydraulics.

2. Experimental Technique

[10] The experimental apparatus used in these experiments is shown schematically in Figure 1. The equipment

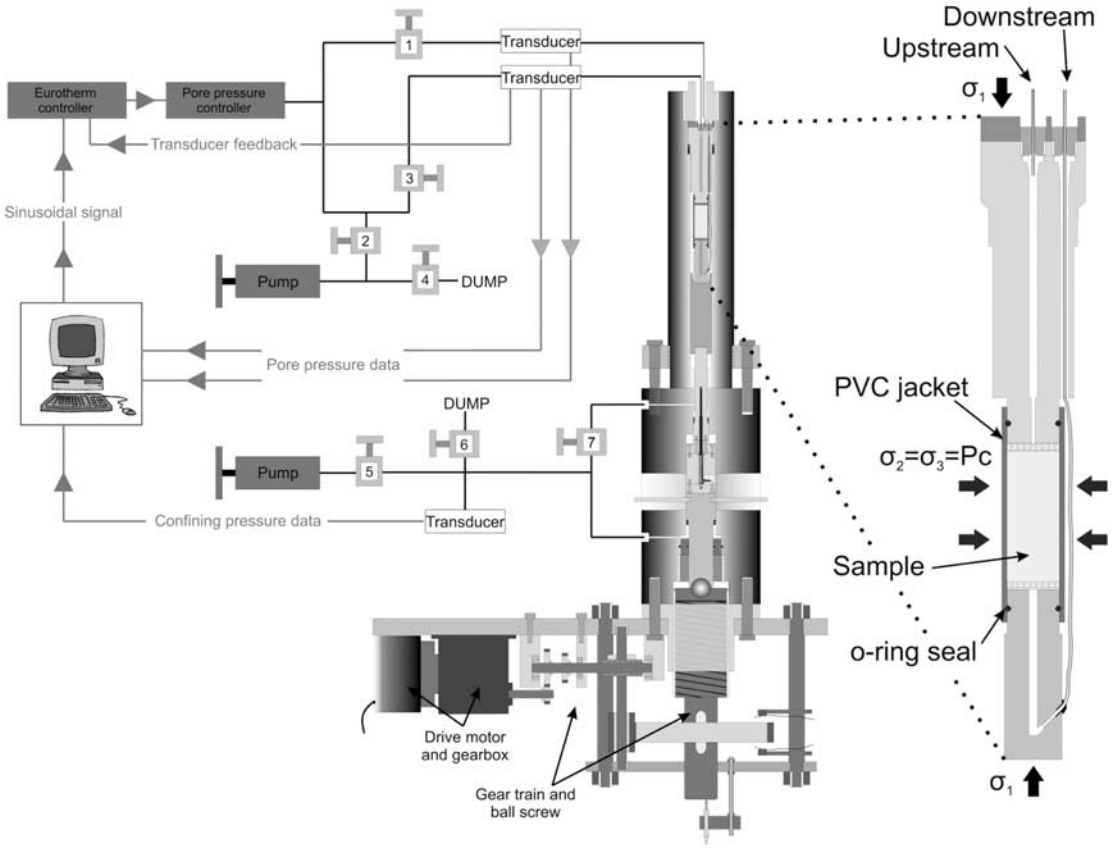

Figure 1. Schematic diagram of the experimental apparatus. The pore pressure oscillation technique was used to measure progressive permeability development during constant axial deformation.

is a high-pressure triaxial deformation apparatus with a servo-controlled axial loading system and pore fluid pump. This rig is capable of performing triaxial deformation experiments at confining pressures up to 250 MPa (using silicon oil as the confining medium), measuring permeability down to 10^{-22} m^2, and resolving sample volume changes of less than 0.1 mm^3 in samples with porosities lower than 1%. The upstream pore pressure is servo-controlled and the downstream end of the sample is connected to a low volume reservoir. The pressure transducers have a resolution of 50 Pa. Axial load is measured by a calibrated internal force gauge with a resolution of just under 10 N. Displacement was measured externally using a displacement LVDT in contact with the moving piston. The stiffness of the loading system is 119 kN/mm (at zero confining pressure) and the axial displacement of the sample was obtained by subtracting the displacement of the loading system from the apparent displacement measured by the LVDT. Axial strain was then calculated with reference to the initial length of the sample.

[11] The pore pressure oscillation technique was employed to monitor permeability during experiments. The method was developed concurrently by *Kranz et al.* [1990] and *Fischer* [1992] and is able to measure both permeability, k, and storage capacity, S, simultaneously during the course of a deformation experiment. The technique utilizes the attenuation (amplitude shift) and phase shift of a forced sinusoidal pressure wave created in the upstream reservoir as it is transmitted through the sample to the downstream reservoir to obtain two dimensionless parameters which may be used to calculate k and S [*Fischer*, 1992]. Recently *Bernabe et al.* [2006] reanalyzed the pore pressure oscillation technique, showing that when the sample storage capacity is small compared to that of the downstream reservoir, it is difficult to resolve the sample storage capacity, although high-resolution values for permeability may still be obtained using an approximate solution of the diffusion equation with the appropriate boundary conditions. The downstream storage capacity of the pore fluid system is 9.4×10^{-16} m^{3}Pa^{-1}, which is suitably small enough to allow permeability to be accurately determined. The improvements of *Bernabe et al.* [2006] have been incorporated into the processing of the data in this study.

[12] The advantage of using this technique to measure permeability is that as long as any changes in permeability are small relative to the time required to collect sufficient data for processing, permeability may be continuously monitored throughout an experiment. Additionally, any changes in the sample pore volume that will result in pore pressure changes can be processed out as long as the change is sufficiently long in comparison to period of the sinusoidal pressure oscillation. A minimum of two waveforms are required to be able to calculate the permeability. Given that, for the typical initial low permeability of the rocks used in this work, the period of the pressure oscillation is ~3000 s, the experiments were conducted with a low strain rate so that any changes in the permeability as a result of the deformation would occur on a much longer timescale than

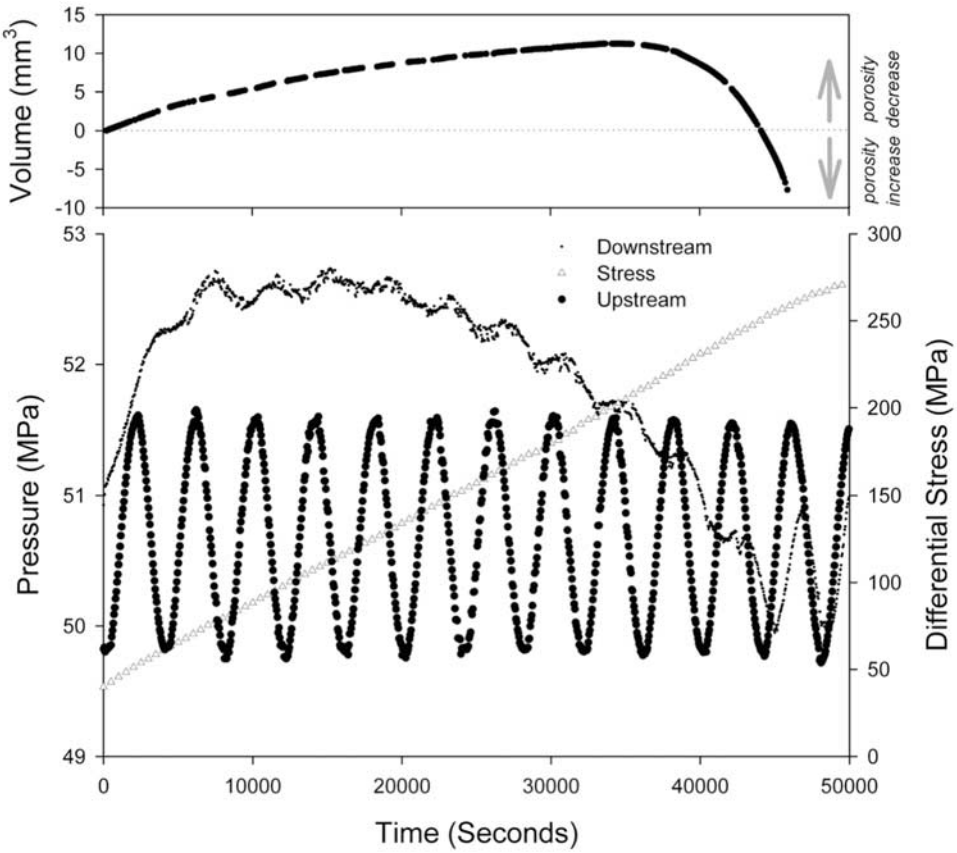

Figure 2. Typical raw data experimental results from a permeability measurement experiment during axial loading. The data stops just before macroscopic failure of the sample as failure occurs very quickly and the pore pressure oscillation technique cannot be used (see text for more detail). The volume is the change in sample volume, determined from the amount of fluid that moves in or out of the sample during deformation as measured by the volumometer. The mean long-term changes in downstream pressure are removed before permeability processing. See text for details.

the period of oscillation. The axial strain rate was kept constant at 9×10^{-8} s^{-1} during all experiments.

[13] Samples were saturated with deionized distilled water and placed in a PVC jacket. Porous alumina spacers are inserted on to the upstream and downstream faces of the sample which ensures that there is an even distribution of pore pressure across the face of the sample. The upstream pore pressure (P_p) was kept controlled with oscillations with an amplitude of 1 MPa around a mean of 50 MPa and the confining pressure P_c ($=\sigma_3$) was varied between 60 and 100 MPa to explore the effect of various effective pressures on the permeability evolution. The oscillating wave is assumed to have a negligible effect on the damage mechanics in the sample. The servo-controlled pore fluid pump maintained oscillating pressure wave, and the pore volume change was recorded by monitoring the piston displacement using a displacement LVDT. Once the specified confining and pore pressures were attained, the oscillating upstream pressure wave was enabled and once equilibrated (i.e., downstream pressure began to show a noticeable pressure wave around a constant mean), differential load was applied via a servo-controlled loading system as described above and shown in Figure 1.

[14] During processing the permeability was calculated from every data point in the data file from the corresponding end point two waveforms later. The resultant value for permeability is an average over these two waveforms, which means that permeability values are somewhat smoothed and rapid variations will not be detected. Figure 2 shows a typical data file from an experiment on granodiorite during axial loading at a constant strain rate up to sample failure. The upstream pore pressure is servo-controlled to produce the pressure oscillation around a mean. The mean downstream pore pressure varies throughout the experiment, due to the change in volume created by microcrack closure and dilatancy. These changes in mean downstream pressure are removed from the experimental data during processing by assuming a constant rate of pressure change between the start and end of each cycle and removing fractions of difference by linearly interpolating the change for each point in the record between the start and the end of the cycle [*Faulkner and Rutter*, 2000].

[15] The material used for experiments were rock cores of 20 mm in diameter and 50 mm in length were cut from intact rock blocks of Westerly granite and Cerro Cristales granodiorite. They were placed in the sample assembly as shown in Figure 1. Westerly granite (from southeast Rhode Island, USA) is commonly used in experimental rock mechanics due to its small grain size and low initial crack density and the fact that it is generally considered to be

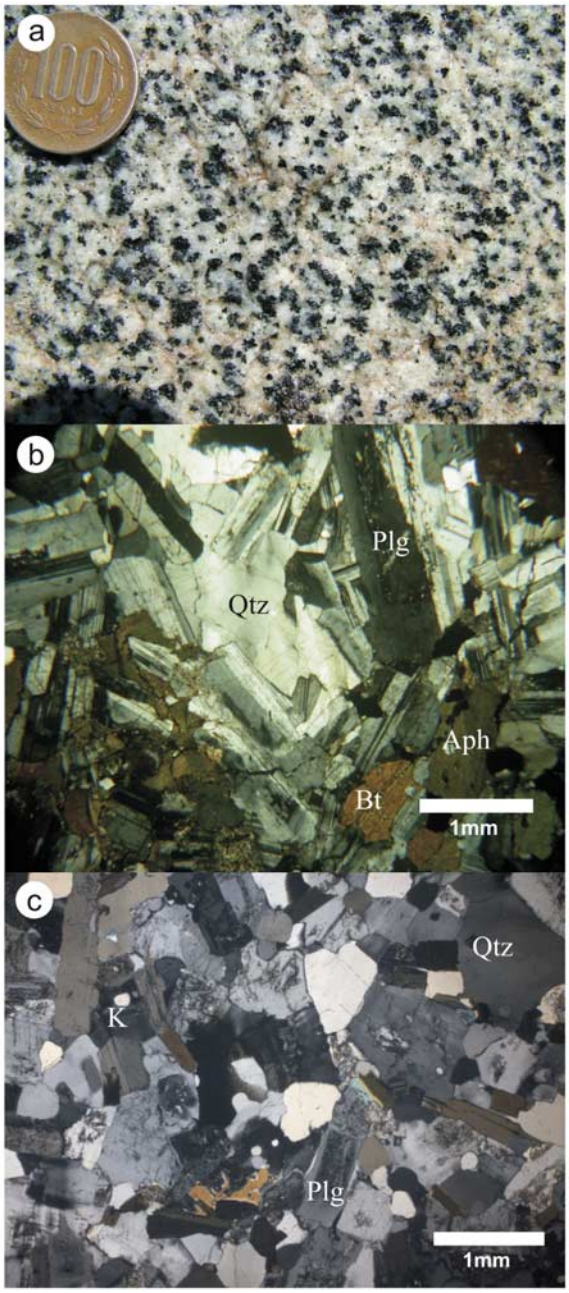

Figure 3. (a) Example of the Cerro Cristales Granodiorite in hand specimen. (b) Thin section of granodiorite in transmitted cross-polarized light. (c) Thin section of Westerly granite in transmitted cross-polarized light. Major phases are labeled. Qtz is quartz, Plg is plagioclase feldspar, Aph is amphibole, Bt is biotite, and K is microcline/orthoclase.

isotropic. Hence it can yield a high level of experiment reproducibility under carefully controlled test conditions [see *Lockner*, 1998; *Haimson and Chang*, 2000]. The grain size of Westerly granite varies from 0.05 to 2 mm (see *Moore and Lockner* [1995] for more detailed description) and has a porosity of around 1% [e.g., *Brace*, 1965]. Average modal grain size in the Westerly samples in this study was 0.5 mm, consisting of microcline, plagioclase, quartz and mica. The Cerro Cristales granodiorite (Figure 3) is taken from the Cerro Cristales pluton in the Coastal Cordillera region of the Atacama desert in Northern Chile, which was first described by *Uribe and Niemeyer* [1984]. This pluton has been studied in detail by *González* [1990, 1996, 1999] and consists of plagioclase, quartz, orthoclase, biotite, and amphibole with an average modal grain size of 0.7 mm and intact porosity is between 2 to 6%.

[16] The rationale behind using Cerro Cristales granodiorite in addition to Westerly granite is that microfracture densities have previously been measured in natural samples [e.g., *Faulkner et al.*, 2006], and future work will aim to quantify experimentally induced microfractures and associated permeability measurements, and relate to these to a natural fault zone. Westerly granite provides an excellent comparison for the granodiorite results.

3. Results

[17] The experimental details for all of the tests reported are summarized in Table 1. In this section, comparisons are made between the variations in permeability during progressive deformation until failure of samples of granodiorite and granite at various effective pressures. In order to investigate how the permeability hysteresis varied at different points in the strain history, one sample was also subjected to increasing-amplitude cyclic loading (see Table 1). This consisted of five increasing and decreasing stress cycles with increasing peak stresses of 60, 70, 80, 90, and 100% of the failure stress for each cycle, with the lower limit of each cycle at 15% of the failure stress.

[18] All samples of both rock types showed localized brittle failure in the form of a throughgoing shear fracture (Figure 4a) at an acute angle to the greatest principal stress, and increased microfracture damage (Figure 4b). Figure 4 shows fracture damage seen in a deformed Westerly granite sample and shows very similar fracture damage to that seen in Cerro Cristales samples. Results for Cerro Cristales granodiorite are first presented, followed by results of Westerly granite, and then results of the increasing amplitude cyclic loading test on Westerly granite.

3.1. Cerro Cristales Granodiorite

[19] Figure 5 shows differential stress and permeability plotted against axial strain for the six tests completed on Cerro Cristales granodiorite at effective pressures of 10, 25, and 50 MPa. The stress-strain curves show typical behavior of crystalline rock with peak stress increasing

Table 1. Summary of the Conditions and Key Mechanical Results From the Triaxial Experiments

Rock Type	P_{eff} (MPa)	P_c (MPa)	P_p (MPa)	Peak Stress (MPa)	Test
Westerly granite	20	70	50	356	9
Westerly granite	15	65	50	330	10
Westerly granite	10	60	50	278	7
Westerly granite	10	60	50	276	8[a]
CC. Granodiorite	50	100	50	350	1
CC. Granodiorite	50	100	50	350	4
CC. Granodiorite	25	75	50	275	3
CC. Granodiorite	25	75	50	290	5
CC. Granodiorite	10	60	50	220	2
CC. Granodiorite	10	60	50	216	6

[a]Test 8 was cycled.

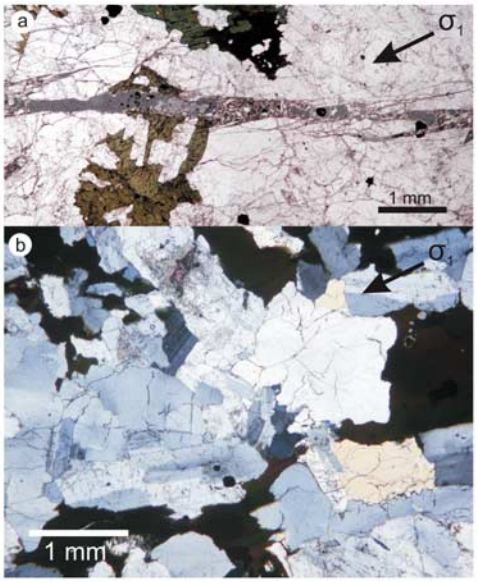

Figure 4. (a) Thin section of experimentally deformed Westerly granite in transmitted plain-polarized light, highlighting a throughgoing shear fracture. This is representative of the shear fractures seen in both rock types. (b) Thin section of experimentally deformed Westerly granite in transmitted plain-polarized light showing diffuse microfracture damage.

with increased confining pressure (or effective stress). For the first 50 MPa of loading the stress-strain response is concave upward, becoming very nearly linear soon after. Stress-strain behavior for all effective pressures then appears to be linear-elastic up to the yield point (where deviation from the linear trend occurs) and then concave down until peak stress prior to sample failure. Peak stresses leading to failure range from around 220, 290 to 350 MPa for effective pressures of 10, 25 and 50 MPa, respectively, with repeat tests at the same pressures showing good reproducibility. For all tests, sample failure occurs very quickly after the peak stress is reached after an increase in strain (sample necking).

[20] Initial preloading values of permeability vary over an order of magnitude from as low as 4×10^{-21} m^2 to 7×10^{-20} m^2. As strain increases, permeability initially decreases for all effective pressures up to a strain of 0.0015, which compares well to the concave upward section of the stress-strain curve. For the lowest effective pressure of 10 MPa, after the initial decrease permeability steadily increases with an increasing gradient up to the peak stress just preceding sample failure, with permeability varying from 3.5×10^{-21} to 9×10^{-19} m^2, over 2 orders of magnitude change. For effective pressures of 25 MPa, the permeability increases relatively slowly up until a strain of 0.0035, where there is a relatively sharp turning point and permeability increases sharply from around 1.7×10^{-20} to 6.3×10^{-19} m^2. For effective pressures of 50 MPa, again permeability increases relatively slowly up to a turning point around a strain of 0.0038, where the permeability changes significantly with an increase from 10×10^{-21} to 1.8×10^{-19} m^2.

[21] Figure 6 shows permeability and pore volume change as functions of differential stress for Cerro Cristales granodiorite. The volume is the amount of fluid that moves in or out of the sample during deformation as measured by the volumometer and is proportional to connected crack volume. By assuming there is a relatively high density of connected microcracks in the sample, then it is possible to use the volume of water that enters or leaves the sample measured by the volumometer as a proxy for relative porosity change. Some studies convert pore volume into volumetric strain relative to the initial intact sample volume, but this relies on the extra assumption that there is no elastic strain within the crystals. Positive volume change therefore indicates pore fluid being added to the sample (increase in porosity) and negative change is pore fluid being expelled (decrease in porosity) from the sample. The stress-permeability relationships are similar to the relationships for strain versus permeability shown in Figure 5, as might be expected, although the curves for the repeated tests at the same effective pressures are slightly spread out due to small variations in the peak stress. For all tests, the pore volume initially decreases up to the turning point at which it then begins to increase at an accelerating rate. One key observation is that the inflection point of the volume-stress curves, i.e., where the porosity stops decreasing and starts increase, does not coincide with

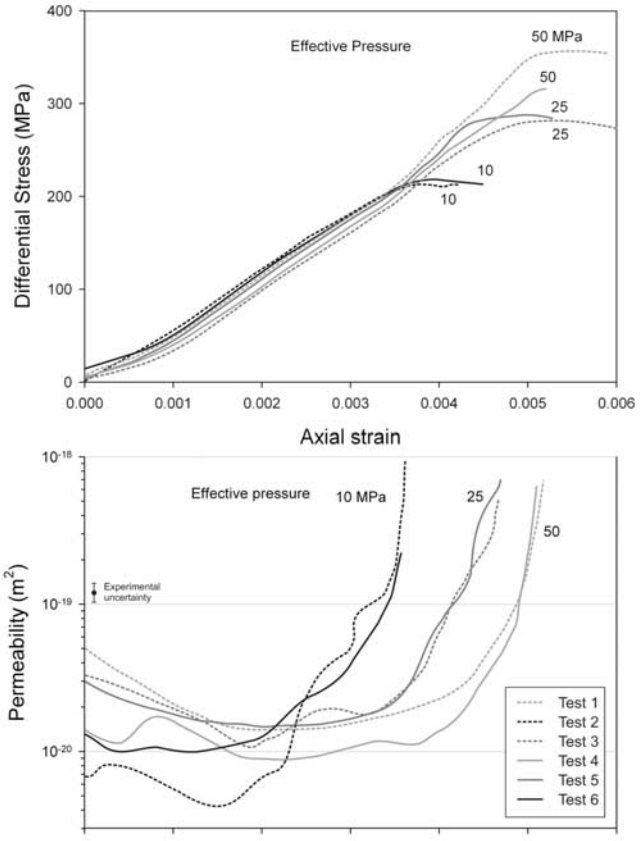

Figure 5. Experimental data for Cerro Cristales Granodiorite. The differential stress and permeability are plotted versus axial strain. Effective pressures are indicated, and pore fluid pressure (deionized water) was maintained at 50 MPa. Test numbers refer to those used in Table 1. A range of experimental uncertainty is shown. This represents the scatter that was present in the processed permeability data.

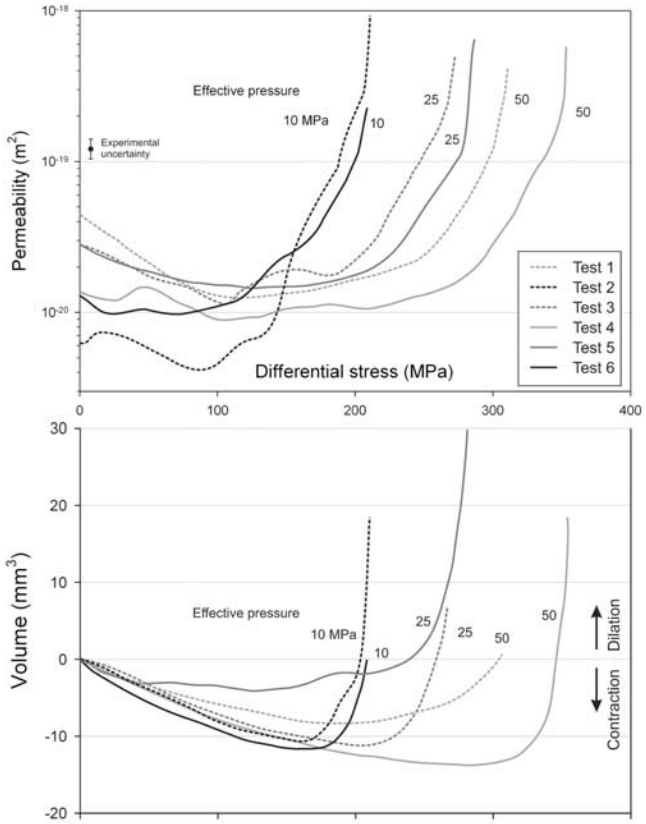

Figure 6. Permeability and sample volume change as functions of differential stress for Cerro Cristales granodiorite. Water pore pressure is maintained at 50 MPa. The range of experimental uncertainty represents the scatter that was present in the processed permeability data.

the inflection point of the permeability-stress plot. Permeability begins to noticeably increase at an appreciably lower strain.

[22] Figure 7 shows a graph of differential stress and permeability plotted versus time for tests 2 and 3 on Cerro Cristales granodiorite. Postfailure permeability values have also been measured and plotted for these two tests, where there has been a substantial drop in the differential stress. Postfailure permeabilities were not measured in all samples. The interpretation of the postfailure permeability data is not straightforward as the sample will have developed a highly heterogeneous permeability structure during the formation of the shear fracture. As a sample approaches the peak stress and failure is imminent, there is a small time window where no data can be gathered as the final stage of the loading between peak stress and the failure stress occurs very rapidly making it difficult to gain results for permeability in such a short space of time. The period of the oscillation wave is reduced during the experiment (from 5000, 2000, 1000, 500, 250, and 100) as the sample becomes more permeable, and the period is relatively small toward the end of the experiment, so only a small segment of data will be missing. However, it can be seen that postfailure permeability is higher for both tests. For an effective pressure of 10 MPa, permeability reaches as high as 4×10^{-18} m^2 which is 3 orders of magnitude change from the initial preloading permeability. An additional consideration is that data on permeability change immediately preceding macroscopic sample failure cannot be recorded. As the data show that permeability increase is accelerating approaching failure the observed permeability increase of 2 orders of magnitude should be considered a lower limit.

3.2. Westerly Granite

[23] Figure 8 shows the differential stress versus axial strain for the three tests conducted on Westerly granite at effective pressures of 10, 15, and 20 MPa. Owing to the higher compressive strength of the Westerly granite in comparison to the granodiorite, effective pressures were not taken higher than 20 MPa (70 MPa confining pressure) as the failure stress could not be reached due to it being beyond the maximum load capacity of the loading apparatus. As was found for the granodiorite, the stress strain curves for Westerly granite show typical behavior for crystalline rock with peak stress increasing with increased effective pressure. The stress-strain response is concave upward for the first 40 MPa load, becoming very nearly linear soon after. Stress-strain behavior for all effective pressures then becomes linear elastic up to the yield point and then slightly concave down until peak stress prior to sample failure. The peak stresses are 278, 330, and 356 MPa for effective pressures of 10, 15, and 20 MPa, respectively (Table 1).

[24] Starting values of permeability range from 3.6×10^{-20} to 6×10^{-20} m^2, which are toward the upper range and slightly higher than the starting permeability of Cerro Cristales granodiorite. This range in permeability does not vary as much as the Cerro Cristales granodiorite, but this is likely to be due to the smaller range of effective pressures used. In contrast to the Cerro Cristales granodiorite, as strain increases, there is a very small decrease, if any, in

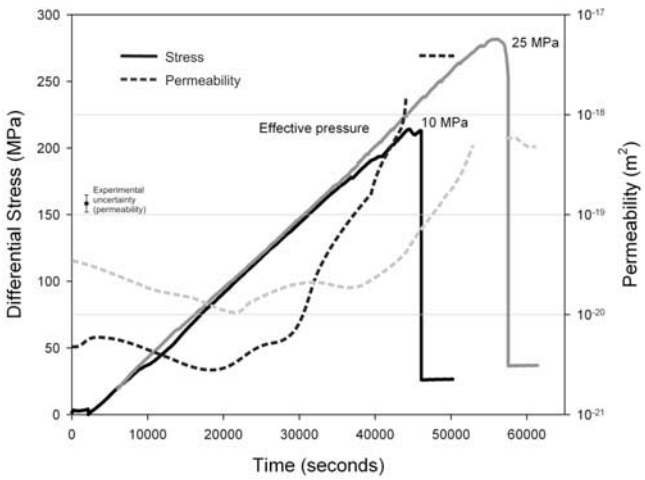

Figure 7. Experimental data for Cerro Cristales Granodiorite tests 2 and 3 at effective pressures of 10 and 25 MPa. The differential stress and permeability are plotted versus time and include measurements of permeability in the postfailure region. Pore fluid pressure was maintained at 50 MPa. The range of experimental uncertainty represents the scatter that was present in the processed permeability data.

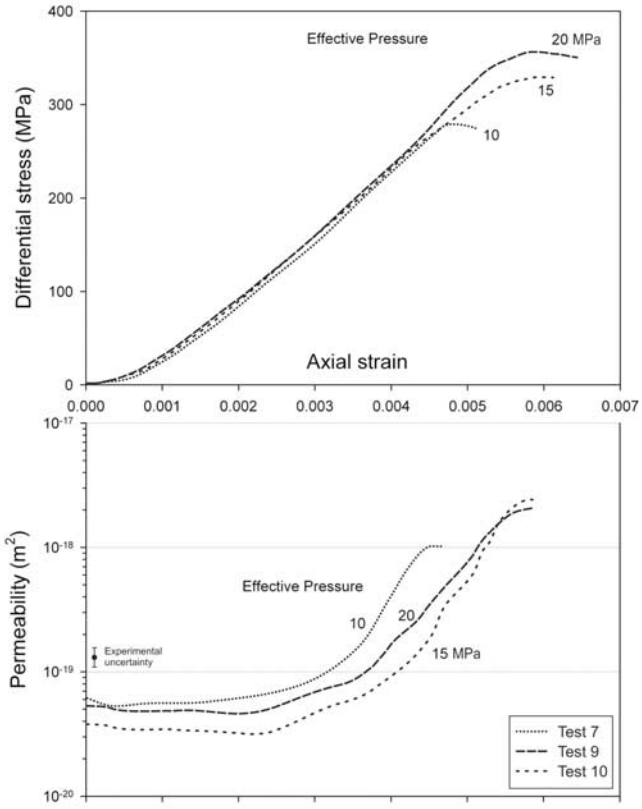

Figure 8. Experimental data for Westerly Granite. The differential stress and permeability are plotted versus axial strain. Effective pressures are indicated, and pore fluid pressure was maintained at 50 MPa. Test numbers refer to those in Table 1. The range of experimental uncertainty represents the scatter that was present in the processed permeability data.

permeability during the initial nonlinear section of the stress strain curve. As with the granodiorite, permeability steadily increases and accelerates prior to sample failure.

[25] For the lowest effective pressure of 10 MPa, permeability steadily increases at a strain of around 0.002 from 5×10^{-20} to 1×10^{-18} m^2, just over an order of magnitude. For effective pressure of 15 MPa, the permeability begins to rise at a strain of 0.0027 from 3.3×10^{-20} to 2.5×10^{-18} m^2. For the highest effective pressure of 20 MPa, permeability begins to rise at a strain of 0.0033 from 4×10^{-20} to 2×10^{-18} m^2. Unlike the granodiorite, there is no relationship between the final prefailure permeability and effective pressure. In fact the lowest effective pressure appears to be associated with the smallest change in permeability.

[26] Figure 9 shows permeability and pore volume change as functions of differential stress for Westerly granite. The stress-permeability relationships are similar to the relationships shown in Figure 8 for strain and permeability. The volume-stress curves suggest volume initially decreases, and hence porosity decreases, to a peak level that corresponds well with the onset of steepening gradient of the permeability curve. This contrasts with the results from the Cerro Cristales granodiorite that showed the permeability began to increase slightly before the volume began to increase. The turning point/yield stress increases as a function of effective pressure at 130, 155, and 180 MPa for effective pressures of 10, 15, and 20 MPa, respectively. The peak volume, i.e., maximum decrease in porosity, also seems to vary as a function of effective pressure, with the largest volume increase of around 12 mm^3 for an effective pressure of 20 MPa. This volume decrease is comparable to that of the Cerro Cristales Granodiorite.

3.3. Increasing Amplitude Cyclic Loading Test on Westerly Granite

[27] In addition to the tests described above, an increasing amplitude cyclic loading test was completed on Westerly granite in order to identify any permeability hysteresis due to the loading and unloading of stress within a sample. This was done in an attempt to examine what effect such loading histories may have on in situ materials that undergo loading cycles such as in earthquake events or during fault formation. Westerly granite was used for this experiment to enable comparisons with existing cyclic studies on Westerly. Figure 10a shows a graph of differential stress versus axial strain for an increasing stress amplitude cyclic loading test on Westerly granite. The sample was systematically loaded and unloaded through five increasing amplitude stress cycles; the maximum

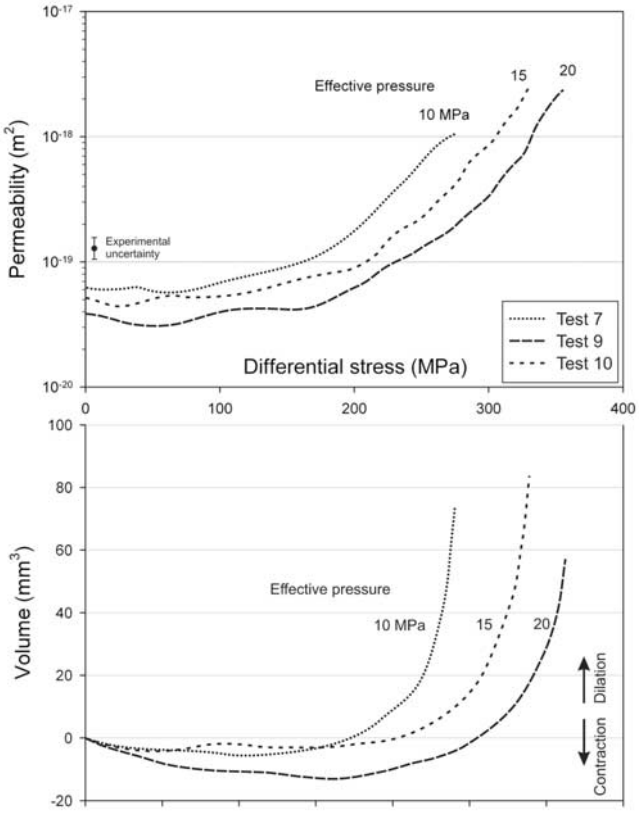

Figure 9. Permeability and sample volume change as functions of differential stress for Westerly granite. Water pore pressure is maintained at 50 MPa. The range of experimental uncertainty represents the scatter that was present in the processed permeability data.

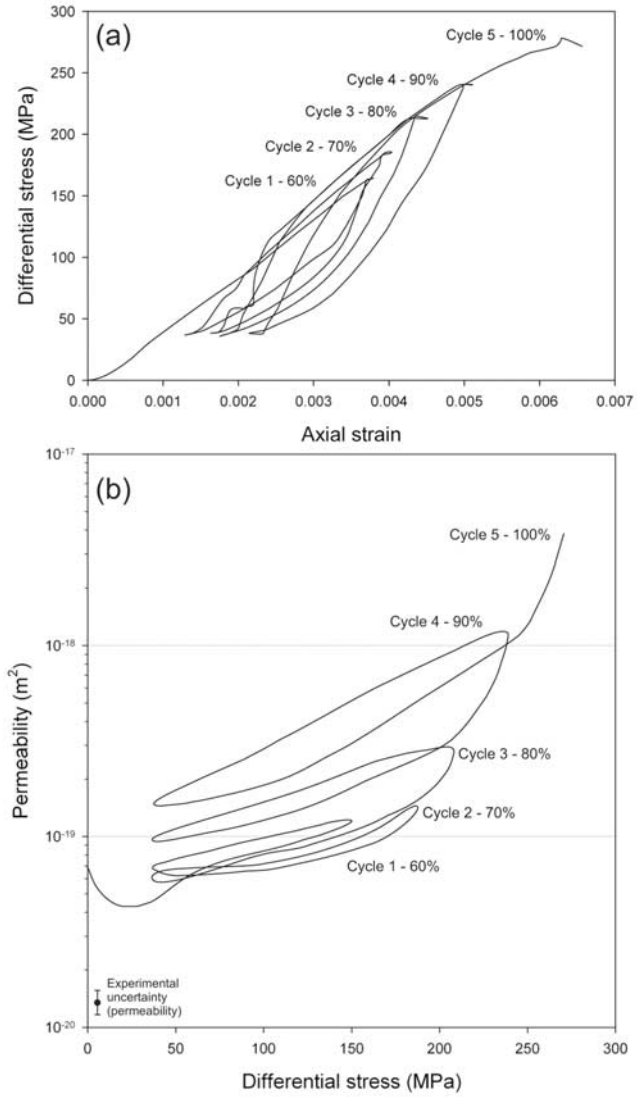

Figure 10. Experimental data for stress cycled Westerly granite. Each cycle is labeled and the approximate percentage of the failure stress of each cycle is indicated. Pore fluid pressure (water) was maintained at 50 MPa with a confining pressure of 60 MPa. (a) Differential stress versus axial strain. (b) Permeability versus differential stress. The range of experimental uncertainty represents the scatter that was present in the processed permeability data.

stress achieved for each loading cycle before unloading started at 60% of the failure stress for the first cycle, and each subsequent cycle maximum stress was increased by approximately 10% of the failure stress till sample failure. Each unloading cycle was stopped at around 15% of the failure stress. A cumulative increase in strain with each cycle can be seen by examining the base of each unloading cycle, which suggests that permanent strain has accumulated between each cycle due to the accumulation of crack damage. Figure 10b shows a graph of permeability versus differential stress for the same cyclic test as shown in Figure 10a. For the first two cycles (up to 60% and 70% of the failure stress) the permeability increases with increasing differential stress and follows the same path on unloading, but the trend is largely reproduced between the cycles (Figure 10b). This implies the stress is not high enough to promote crack development at this stage. Above 70% of the failure stress, the permeability increases between each cycle and shows hysteresis. During the first loading cycle, the permeability decreases slightly from an initial permeability of around 7×10^{-20} m^2, again presumably due to the closure of preexisting cracks. As differential stress increases, the permeability increases correspondingly to 1.4×10^{-19} m^2 at the top of the stress cycle (60% of the failure stress). The second cycle (70% failure stress) follows a very similar permeability-stress path to the first. The third cycle (80% failure stress) however shows an increase in permeability of 500%, with the permeability gradient steepening somewhat at higher stress. As differential stress is removed during unloading, the permeability is initially maintained but then begins to decrease as the differential stress is reduced. The concave-up shape of the loading-permeability curve is mirrored in the unloading curve and the permeability at the bottom of the cycle is 300% higher than the starting permeability. The fourth cycle (90% failure stress) shows a permeability change of more than 1000% (an order of magnitude), and the permeability at the end of the cycle is 400% higher than the permeability at the start of the cycle. The fifth and final cycle also shows a permeability increase of over 1000% up to sample failure, with the final prefailure permeability being almost 2 orders of magnitude higher than the initial permeability, at 4.4×10^{-18} m^2.

4. Discussion

[28] In the majority of the discussion, we relate our data to natural fault damage zones. It may at first seem unusual that our data on permeability evolution during the phase of progressive deformation that precedes fracture localization and faulting is applied to preexisting fault systems. However, the rocks in the microfracture damage zone surrounding the fault core have never experienced stresses high enough to result in failure; hence our data are directly applicable to these regions.

[29] In this section, differences in the strength and permeability evolution of Cerro Cristales granodiorite and Westerly granite are first discussed. Next, the permeability evolution induced from cyclic damage is discussed, and in light of these changes in permeability, the crack network controlling this permeability change is addressed. Potential fault zone healing and permeability recovery is then discussed in light of the permeability changes shown in the results, followed by an examination of the relative fluid flow between macrofractures and microfractures. A summary model for the strength and permeability evolution of crystalline rocks during progressive deformation is then presented, along with discussion on the implications for crustal fluid flow and fault zone hydraulics.

4.1. Comparison of the Strength and Permeability Evolution of Cerro Cristales Granodiorite and Westerly Granite

[30] The stress-strain relationships show that Westerly granite appears to be much stronger than Cerro Cristales

granodiorite (summarized in Table 1). Although the mineralogy between the two rock types is not dramatically different, Westerly granite has slightly smaller average grain size (Figure 4), and this may contribute to the difference in strength as the average microcrack size is probably smaller, since lengths are commonly governed by the grain size.

[31] The permeability results show many similarities between the two rock types. With increased differential stress and strain, there appears to be an initial transient of permeability decrease that is more apparent for the Cerro Cristales granodiorite than the Westerly granite. The initial decrease is related to the nonlinear increasing stiffness part of the stress-strain curve, most likely due to the closure of microfractures orientated obliquely and transversely to the applied load. Crack closure causes a decrease in porosity and related decrease in permeability. The Westerly granite shows no significant decrease in permeability in the crack-closure phase, which suggests that the crack network is not hydraulically well-connected. Also, the apparent lack of discernable decrease in permeability of the Westerly granite may be because the Cerro Cristales granodiorite contains larger microcracks, as discussed above. It may also partly be due to the Cerro Cristales granodiorite samples being cored from surface-derived rocks, whereas the Westerly granite was cored from quarry cut samples. If there are cracks that have weathering products in them within the Cerro Cristales, then these may hold open the cracks until a small amount of shear helps to close them. The confining pressure will play a part in how well these shearing cracks will close, hence the influence the confining pressure has on the permeability results for Cerro Cristales granodiorite.

[32] As noted in the results, the inflection point of the volume-stress curves for the Cerro Cristales, i.e., where the porosity stops decreasing and starts to increase, does not coincide with the inflection point of the permeability-stress plot, suggesting that permeability is increasing noticeably at an appreciably lower strain. This is a key observation, and is entirely to be expected, since compaction and dilatancy are not mutually exclusive processes. Cracks in orientations at high angles to σ_1 continue to close while new dilatant cracks grow subparallel to σ_1. The axial orientation of the new dilatant cracks means that they contribute more to axial permeability than the compacting radial cracks. Hence, the increase in permeability precedes the decrease in crack volume.

[33] The effective pressure has an influence on several aspects of the sample behavior. For the Cerro Cristales granodiorite, the permeability immediately prior to failure appears to scale with effective pressure, with tests run at higher effective pressure showing lower peak permeability (Figure 6). This may be due to higher effective pressures having a greater closing effect on axially orientated microcracks. This inference is supported by the lower pore volume increase in the tests conducted at higher effective pressures. However, the Westerly granite data do not show as clear a relationship between prefailure peak permeability and effective pressure. Effective pressure also has some effect on the shape the permeability strain curves, with an increasingly sharper turning point with increasing effective pressure (Figures 4 and 7).

[34] As shown in Figure 7, the postfailure permeabilities for two of the samples showed permeability variation of 3 orders of magnitude. Permeabilities immediately following shear failure in triaxial experiments are often seen to be high. This has previously been interpreted as being due to both to the generation of a throughgoing fracture (e.g., Figure 4a) that can act as a conduit for fluid flow and to transient shear heating of the pore fluid due to the rapid shear displacement. The latter phenomenon can lead to a temporarily increased pore fluid pressure and hence an apparent temporary increase in permeability. However, as the fault evolves with further shear displacement, a well-packed gouge of comminuted material with a wide particle size distribution (commonly described as a fractal distribution) will be developed, and this commonly leads to a progressive decrease in permeability until some steady value is eventually reached. While we do see almost 3 orders of magnitude change in permeability postfailure, this has to be interpreted with caution as measurements made very close to the dynamic rupture are inherently unreliable because of the transient conditions.

[35] Finally, we note that the there is a larger increase in porosity for the Westerly granite experiments in comparison to those for the Cerro Cristales granodiorite (Figures 5 and 8). This might be related to a denser or more pervasive crack network forming in the Westerly granite which could be a function of Westerly granite's smaller grain size, especially if cracks are intragranular.

4.2. Permeability Evolution From Induced Cyclic Damage

[36] Rocks do not show perfectly elastic stress-strain behavior, as once the yield point is exceeded there is hysteresis, which implies that some of the energy stored during loading has been dissipated into the specimen [*Jaeger et al.*, 1969; *Paterson and Wong*, 2005]. In low-temperature experiments this energy is generally assumed to be used to create new crack surface area which has a direct effect on both porosity and permeability. The results of the increasing amplitude cyclic loading test on Westerly granite show both strain and permeability hysteresis related to each stress cycle (Figure 10). The total change in permeability is similar to the total change of the noncycled tests, suggesting that the prefailure peak permeability is the same for cycled and noncycled tests and that permeability is primarily controlled by the maximum stress that the sample has experienced rather than number of cycles. The shape of the curve for each stress cycle is very similar with the gradients of the unloading curve showing a very similar pattern. This means that the permeability change with varying differential stress is predictable; the sample can be taken to any percentage of the failure stress and an estimate can be made for the permeability path during unloading.

[37] *Zoback and Byerlee* [1975] determined the permeability of Westerly Granite under cycled stepwise increased axial stress at effective pressures of 39 and 14 MPa (with a pore fluid pressure of 11 MPa) using the pulse transient technique of *Brace et al.* [1968]. These effective pressures are slightly higher than the 10 MPa used for the cyclic loading test in this study. Figure 11 shows the results of *Zoback and Byerlee* [1975] overlain onto the same results from Figure 10b. A key difference between our study and that of Zoback and Byerlee's is that their samples were loaded up to a maximum differential stress of only ~80% of

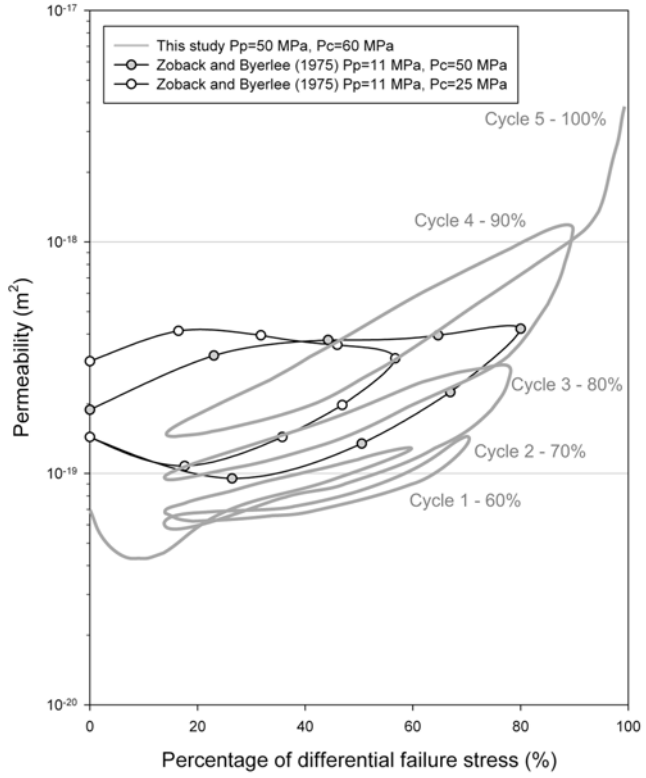

Figure 11. Experimental data for stress cycled Westerly Granite, as shown in Figure 10 but with the results of *Zoback and Byerlee* [1975] overlain for comparison. To aid comparison between the data sets, the permeability has been plotted as a function of the percentage of failure stress.

the failure stress. The form of the two data sets compare well although starting permeabilities for their samples are slightly higher. *Zoback and Byerlee* [1975] preloaded their samples to unspecified high differential stress over 20 times before starting their permeability measurements in an attempt to simulate more closely in situ materials that may repeatedly undergo large stresses, whereas in this study samples are initially intact. This may explain the difference between the starting permeability. A key difference is that where this study has taken stress to levels above 80% of the failure stress, permeability increases by over an order of magnitude before failure.

[38] *Heap and Faulkner* [2008] showed that cyclic fatigue is not a major contributor to microfracture damage in Westerly granite, as constant amplitude stress cycles produced no variations in elastic properties. This was interpreted as indicating that no additional microfracture damage is imparted in the sample. It is only with increasing amplitude stress cycles that further damage is created; until the previous cycle peak stress is exceeded, no new microfracture damage is noticeably introduced. This behavior has been termed the "Kaiser effect" and is supported by acoustic emission analysis during experiments [*Lavrov*, 2003]. Therefore despite the samples of *Zoback and Byerlee* [1975] being cycled 20 times, the results in this study compare well as cyclic fatigue is not very effective without increases in differential stress for each cycle.

[39] Whereas the stress-permeability curves during loading show a concave-up shape, during unloading they show a much shallower gradient resulting in a concave down shape (Figure 11). *Zoback and Byerlee* [1975] attribute this increase to two competing effects that determine the permeability; flow decrease through the axial cracks as they begin to close, but flow increases through the opening nonaxial cracks. In their study, they saw a slight increase in permeability as differential stress was decreased which they interpret as the nonaxial cracks temporarily dominating the behavior of the sample.

[40] The experiments in this study were completed at room temperature with water as a pore fluid, unlike *Zoback and Byerlee* [1975] who used argon. As water is arguably the most common geofluid in the upper crust, the results of this study might be viewed as more applicable to natural crustal conditions. However, the data compare well, suggesting processes such as stress corrosion or physicochemical effects of the pore fluid do not have a large effect on the permeability of the crystalline material, at least over the range of conditions and timescales under which the experiments were performed. It also important to note from the comparison of the data in this study with that of *Zoback and Byerlee* [1975] shown in Figure 11, the pulse transient method of measuring permeability and pore pressure oscillation technique appear to produce similar results. However, the continuous measurements obtained using the pore pressure oscillation technique give a more complete data record which is particularly useful for detailing the more subtle permeability changes during loading and unloading in cycles 1 and 2.

4.3. Crack Network Controlling Permeability

[41] As faults in brittle rock are shear fractures formed through the interaction and coalescence of many tensile microcracks [*Lockner et al.*, 1991; *Lockner et al.*, 1992; *Reches and Lockner*, 1994; *Healy et al.*, 2006], an increasingly heterogeneous microfracture network must develop as a sample approaches failure. In this study we have measured and reported increases in bulk permeability with increasing differential stress and it is important to understand the heterogeneity of the microcrack network at various points in the sample's deformation history. If a highly heterogeneous crack network develops early, then the reported bulk permeability data will not reflect the complexity of the permeability structure. [*Lockner et al.*, 1991] presented observations of quasi-static fault growth in Westerly granite, where the formation of a shear fracture was monitored by located acoustic emission (AE) events by subjecting an initially intact sample of granite to increasing differential stress until sample failure. They showed that the prefailure region of the stress-strain curve, the same region in which permeability was measured in this study, corresponds to relatively diffuse acoustic emission events that are interpreted to be homogenous microfracturing occurring through the sample. It is only around the failure stress that localization quickly develops and sample failure occurs. From this we infer that the variation of permeability seen prefailure is entirely due to a relatively homogenous microfracture network developing throughout the sample, and hence our bulk permeability data are representative. However, it must be noted that the fracture

network does become increasingly anisotropic throughout the prefailure loading curve. Increasing the differential stress has two effects: (1) it preferentially closes preexisting cracks oriented normal or subnormal to σ_1, and (2) it preferentially generates new dilatant cracks parallel or subparallel to σ_1. Thus, even if the rock has an initially isotropic permeability, it can become increasingly anisotropic as deformation proceeds. Such anisotropy is also seen around natural fault zones, as opening mode microfractures form in an orientation perpendicular to the local minimum compressive principal stress direction [*Friedman*, 1963; *Engelder*, 1974; *Wilson et al.*, 2003].

4.4. Fault Healing and Permeability Recovery

[42] While the experiments completed in this study were completed at room temperature, within the seismogenic zone of the crust, elevated temperatures in hydrothermal systems are known to affect the permeability of fault zones with time. If we wish to relate the experimental data in this study to natural fault zones, we must consider such permeability recovery processes. *Sibson* [1996] highlighted that a large proportion of the structural permeability developed in the fault-fracture meshes is likely to be transient. This is because microcracks, fractures, and faults may all become infilled with low-permeability hydrothermal precipitates, alteration products, and/or clay-rich gouge. *Tenthorey et al.* [1998] and *Aharonov et al.* [1998] related decreases in permeability to authigenic mineral formation during diagenesis experiments at elevated temperatures. This has particular relevance to understanding earthquake processes, as many recent models of the earthquake cycle invoke the formation of low-permeability minerals seals within fault zones in the interseismic period [e.g., *Blanpied et al.*, 1992; *Byerlee*, 1993; *Lockner and Byerlee*, 1995; *Miller et al.*, 1996]. Such mineral seals may aid the development of high fluid pressure conditions within the fault zone, which is one of the explanations for the apparent weakness of the San Andreas fault that is implied by the lack of a measurable heat flow anomaly [*Brune et al.*, 1969; *Lachenbruch and Sass*, 1980] and orientation of principal stresses driving fault movement [*Zoback et al.*, 1987]. Such results also support the hypothesis that fault seals can form in less time that the recurrence interval for larger earthquakes at the base of the seismogenic zone. Geophysical evidence exists for healing processes, for example the Landers fault zone in California was shown to exhibit time-dependent increase in seismic velocity following the 1992 earthquake, only interrupted by the nearby 1999 Hector Mine earthquake [*Vidale and Li*, 2003]. This healing and compaction of the damaged rocks is thought to be a key process in the temporal weakening of large faults by increasing the pore pressure over time [*Sleep*, 1995].

[43] Previous experimental studies investigating healing properties of fault zones have concentrated on two problems, healing of shear fractures and healing of microfracture networks. One is important for fault zone healing and the other is important for damage-zone healing. *Morrow et al.* [2001] studied the reduction of permeability in granite under hydrothermal conditions. They conducted experiments on Westerly granite at effective pressures of 50 MPa and at temperatures from 150° to 500°C, simulating conditions in the earthquake-generation portion of fault zones. Their experiments showed that a fractured sample of Westerly granite (i.e., sample with a postfailure shear fracture) exhibited a steady decline in permeability due to hydrothermal dissolution and mineral growth, beginning at a value almost 2 orders of magnitude higher than that of the intact sample they tested and reaching a near constant rate of decline after ~30 days. In this period the sample reduced in permeability by over an order of magnitude. The initial permeability values of the samples with a preexisted shear fracture at the beginning of their experiments compare well to the values of permeability shown at sample failure in this study. Hence the results from their study would suggest the samples taken to failure in our work could regain up to 90% of their intact permeability in a relatively short amount of time.

[44] In addition to examining the healing potential of a shear fracture in hydrothermal conditions, the healing potential of the rock mass prefailure also needs to be considered, i.e., before a macroscopic shear fracture develops (Figure 4b). *Brantley et al.* [1990] observed the healing of microcracks in quartz at elevated temperatures and discussed the implications for fluid flow. Their results demonstrated that faster healing rates are observed in smaller cracks, whereas macrofractures will transport most of the fluid volume and seal relatively slowly. Microcracks (e.g., Figure 4b) will allow pervasive penetration of fluid into the rock mass, but heal quickly. This suggests that the prefailure microfractures that cause the 2 orders of magnitude increase in permeability are likely to heal considerably faster than postfailure shear-fracture permeability, suggesting prefailure permeability recovery occurs at a faster rate than postfailure permeability recovery. This is also supported by the results of *Blanpied et al.* [1992], where they inferred that the material either side of a saw cut fault healed, leading to elevated pore pressures and fault weakening. Permeability enhancement through faulting and fracturing in fault-related hydrothermal systems competes with permeability reduction as a consequence of fluid flow and precipitation [*Henley*, 1984]. Hence deformation within fault-fracture meshes, either continual or intermittent, is probably necessary for them to remain effective as high-permeability structural conduits [*Sibson*, 1994].

4.5. Fluid Flow in Macrofractures Versus Microfractures

[45] There are a number of studies that have constrained in situ crustal permeability from indirect sources that provide a useful comparison for our experimental data. *Miller et al.* [2004] suggested that earthquakes can initiate large fluxes of fluid using the "fault valving" process first suggested by *Sibson* [1990]. They modeled aftershock patterns following the 1997 Colfiorito earthquake sequence and interpreted these as being triggered by a high-pressure fluid front that migrated up the fault plane from depth. In this model the fluid flow characteristics of the fault zone, as well as the physical dimensions of the damage zone, were tailored to fit the observations. Values for permeability are calculated to be 4×10^{-11} m^2 in the damage zone of the fault. The results in this study show that stressed crystalline

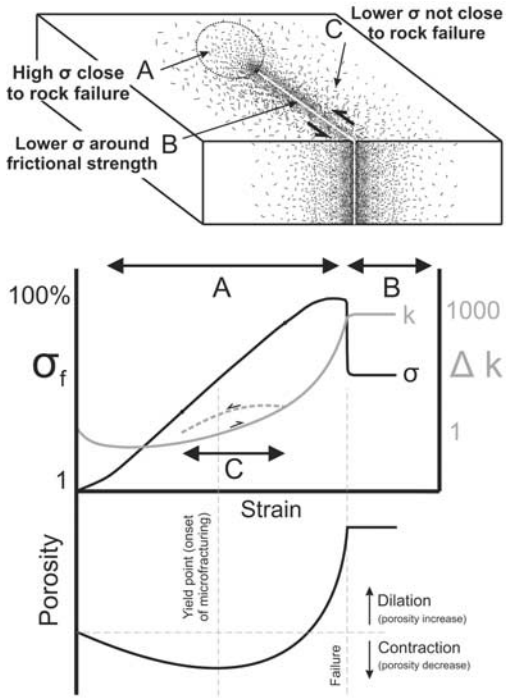

Figure 12. Schematic diagram illustrating relative states of stress and permeability surrounding a fault plane with a highly stressed fault tip and associated microfracture damage. Percentage of the failure stress, permeability, and porosity are plotted as a function of strain. See text for explanation.

rock prefailure has permeabilities nearly 7 to 9 orders of magnitude lower than that predicted by *Miller et al.* [2004] suggesting that such fluid flow rates could not be produced by the pervasive microfracture of the rock matrix. *Manning and Ingebritsen* [1999] inferred permeabilities of 10^{-16} m^2 for crustal permeability in tectonically stable environments, and *Townend and Zoback* [2000] suggested in situ bulk permeabilities of $\sim 10^{-17}$ to 10^{-16} m^2 which is still 1 to 2 orders of magnitude higher than measured immediately before failure in this study. The highest permeabilities measured were those immediately post failure at 4×10^{-18} m^2, which is approaching the suggested crustal permeability of *Townend and Zoback* [2000].

[46] The data presented here support inferences that bulk fluid flow and dilatancy must be dominated by larger-scale structures, such as macrofractures and jointing in the absence of lithological variety. If diffusion models are to be used, then it is important to base these models on macroscale fracture geometries as well as matrix-dominated flow. Experimental studies have demonstrated high permeabilities on the scale of that calculated by *Miller et al.* [2004] in rough fractures in granite and marble, but at low effective normal stress [*Lee and Cho*, 2002]. *Matthai and Belayneh* [2004] used field databased finite element simulations of flow partitioning between fractures and a permeable rock matrix to reveal critical aperture values that mark the transition from matrix- to fracture-dominated flow. They suggested that matrix permeabilities of 0.001–1 D (9.87×10^{-13} to 9.87×10^{-16} m^2) are required for the matrix to either dominate, or contribute significantly to, the total flow. Our measurements are below these suggested values.

4.6. Summary Model for the Strength and Permeability Evolution of Crystalline Rocks During Fault Growth

[47] The schematic graph shown in Figure 12 shows a summary of the key changes in strength and permeability for both rock types. The stress-strain curves become approximately linear once cracks have closed and this is related to the lowest permeabilities measured. Once closed, linear elastic deformation takes place and the permeability either remains constant or slightly increases up to and beyond the yield point. The yield point of the stress-strain curve is commonly defined as the deviation from linear elastic deformation and marks the onset of permanent crack damage. However, as previously pointed out, there are two competing mechanisms throughout deformation, closure of cracks normal to σ_1 and opening of cracks parallel to σ_1. Opening of new dilatant cracks, and the onset of permanent crack damage, commences during the apparent linear phase of deformation (essentially, these two mechanisms are in balance during this phase), as evidenced by the output of acoustic emissions in many published studies [e.g., *Scholz*, 1968; *Sammonds et al.*, 1992; *Cox and Meredith*, 1993]. The deviation from linearity (here called the yield point) is simply the point where the growth of dilatant axial cracks starts to dominate over the compactive closure of radial cracks. We interpret the data in the following way. The rate at which permanent crack damage accumulates increases, at the same time, the rate of closure of preexisting transverse and obliquely oriented cracks slows. Hence the crack growth outstrips crack closure and overall pore volume starts to increase (marked by the turning point in the volume curve), which does not necessarily occur at the yield point. The permeability starts to increase immediately following yield, as new crack growth in an axial direction (and hence favoring axial fluid flow) commences. This occurs even though the overall sample pore volume is still decreasing. In our experiments, this type of behavior is more pronounced for the Cerro Cristales granodiorite than the Westerly granite. From the turning point of the volume curve, as stress and strain increase, pore volume increases dramatically and accelerates up to sample failure. Accordingly, the permeability of the sample shows concomitant increase.

[48] It has been shown both in the field and experimentally that an exponential decrease in microcrack density with distance from a fault plane is commonly recorded around faults in low porosity rock [*Anders and Wiltschko*, 1994; *Moore and Lockner*, 1995; *Vermilye and Scholz*, 1998; *Janssen et al.*, 2001; *Wilson et al.*, 2003; *Faulkner et al.*, 2006]. This is typically interpreted as reflecting a decrease in stress experienced by the rock with distance from the fault core, where stresses will have, at some stage, reached the failure stress. Figure 12 shows a schematic diagram summarizing the permeability structure surrounding a propagating fault tip in crystalline rock assuming a process zone model. The upper diagram shows a three dimensional block with a strike slip fault cutting through it. Microfracture damage surrounds the fault zone, with the most intense microfracture density closest to the fault plane (where differential stress approaches that at failure), and micro-

fracture density decreases with distance from the fault (as the differential stress becomes a progressively smaller fraction of the failure stress). At the fault tip, a process zone (marked as region A) exists, as described above, that relaxes the local stress at the fault tip. This is the prefailure region, where stresses range from low at the edge of the process zone to high at the fault tip. The stress range in this prefailure region is represented by the section marked A on the stress strain curve. In this region, permeability correspondingly increases with increased porosity due to creation of microfracture damage, with the greatest increase in permeability being closest to the crack tip and decreasing exponentially to the edge of the process zone. The variation in permeability could be up to 2 orders of magnitude within this process zone, with the greatest permeability at the fault tip where the rock is approaching failure, and the smallest at the outer limit of the process zone where microfracture damage is at near-background levels. When the stress at the tip reaches critical level and the fracture propagates, there is a corresponding stress drop and the strength of the same area where the fault now exists falls to the frictional strength of the fault (region B). Permeability is greatly enhanced in this shear fracture, and fluid flow initially preferentially occurs here. The results from this study suggest that within this shear fracture the permeability could initially be up to 3 orders of magnitude higher than intact rock permeabilities, although once a small about of shear and a gouge layer is developed, this permeability will be reduced significantly. Conversely, in region C (the damage zone) outside of the newly created permeable shear fracture, the stress drop acts to relieve stress on the microfracture matrix leading to crack closure and reduced permeability. However, as shown in this study, permeability hysteresis due to permanent microfracture damage induced in the rock will mean that permeability is not be reduced to initial levels and can remain somewhat higher. Hydrothermal fluids within the microfracture matrix will work to seal fractures through dissolution and mineralization, while continued fault wear and stress cycling will serve to induce damage in the wall rock surrounding the fault and raise permeability. Microfracture damage surrounding the fault will be representative of peak stress conditions, rather than repeated stress cycling causing cumulative damage.

[49] This schematic model is perhaps easier to apply to relatively young immature macroscopic faults. Such structures are ubiquitous throughout the brittle crust and hence will play an important part in controlling bulk crustal permeability. As faults evolve and grow in size, both the fault core and damage zone will become larger and more complex. However, this model may still be applied to larger-scale faults, as many field studies demonstrate that faults on a range of scales display a consistent exponential decrease of microfracture damage with distance from the fault core [*Brock and Engelder*, 1977; *Chester and Logan*, 1986; *Scholz et al.*, 1993; *Anders and Wiltschko*, 1994; *Vermilye and Scholz*, 1998; *Wilson et al.*, 2003; *Faulkner et al.*, 2006]. However, the permeability structure of larger-scale fault zones is complicated by the presence of secondary subsidiary macroscopic structures related to its formation, each with their own related microfracture distributions.

[50] Finally, we note that the work discussed here applies primarily to faults that crosscut low porosity crystalline rock. Although the enhancements of permeability are significant, lithological variations will have an additional first-order effect on permeability development [*Brace*, 1980], and more experimentation on other rocks is needed.

5. Conclusions

[51] This study presents experimental data on the continuous evolution of permeability pore volume of two crystalline rocks under increasing differential stress. Previous studies have been limited by experimental techniques that require loading to be stopped for permeability to be measured and have considerably fewer measurements. Use of the pore pressure oscillation technique has allowed the measurement of continuous permeability evolution without such limitations.

[52] For both crystalline rocks studied, as differential stress and strain increase, permeability increases by up to and over 2 orders of magnitude up to sample failure. Initially permeability and pore volume decrease with loading then permeability starts to increase followed by a somewhat delayed increase in pore volume. These trends can be explained by the competing processes of axial crack opening and oblique and transverse crack closure.

[53] In tests where postfailure permeability is was measured where shear fractures (macrofracture) had developed in the samples (e.g., Figure 4a), the permeability is over 3 orders of magnitude higher than initial intact permeabilities, as high as 4×10^{-18} m^2 which is approaching measurements of in situ bulk crustal permeabilities of $\sim 10^{-18}$ to 10^{-18} m^2 [*Townend and Zoback*, 2000]. However, this bulk permeability measurement is a product of a highly heterogeneous permeability structure.

[54] Increasing amplitude cyclic loading on Westerly granite shows both strain and permeability hysteresis related to each cycle, with permeability increasing by 400–500% of the starting permeability of each of the first four cycles, with starting permeabilities increasing by 200–300% each cycle. As stress is reduced for each cycle, the permeability is maintained at elevated levels compared to the previous increasing differential load path. Above a peak cycle of 80% failure stress, permeability increases by over an order of magnitude before failure, suggesting that the higher levels of differential stress are very important for permeability evolution.

[55] We infer from previous work that permeability creation will be offset in nature by hydrothermal precipitation at elevated temperatures in a relatively short space of time (e.g., relative to earthquake cycles). Hence repeated fracturing would be required to keep the rock mass acting as viable fluid conduits. Prefailure microfractures that cause the 2 orders of magnitude increase in permeability in the samples are likely to heal considerably faster than postfailure shear-fracture permeability.

[56] The highest permeabilities measured are nearly 7 to 9 orders of magnitude lower than that predicted by high pressure diffusive models such as *Miller et al.* [2004], suggesting that such fluid flow rates cannot be maintained through the pervasive microfracture matrix. Despite 2 orders of magnitude variation in permeability, prefailure permeabilities are still 1 to 2 orders of magnitude lower than inferred in situ crustal permeabilities, although postfailure

permeability approached the lower end of these inferred in situ crustal permeabilities. These comparisons suggest that bulk fluid flow and dilatancy must be dominated by larger-scale structures, such as macrofractures and jointing.

[57] We present a model, based on our data, in which the permeability of a highly stressed fault tip process zone in low-permeability crystalline rocks increases by more than 2 orders of magnitude. Stress reduction related to the onward migration of the fault tip close damage zone cracks, while some permeability is maintained due to hysteresis from permanent microfracture damage.

[58] **Acknowledgments.** We acknowledge financial support from a Natural Environment Research Council grant (NE/C001117/1) to DRF and a University of Liverpool Ph.D. studentship to TMM. John Hakes provided essential technical support in the construction and maintenance of the electronic control systems. We thank Steven Kewin of CAE Services for the construction and maintenance of mechanical components. Thorough reviews from Phil Meredith and an anonymous reviewer helped greatly to improve the manuscript.

References

Aharonov, E., E. Tenthorey, and C. H. Scholz (1998), Precipitation sealing and diagenesis - 2. Theoretical analysis, *J. Geophys. Res.*, *103*, 23,969–23,981, doi:10.1029/98JB02230.

Anders, M. H., and D. V. Wiltschko (1994), Microfracturing, paleostress and the growth of faults, *J. Struct. Geol.*, *16*, 795–815, doi:10.1016/0191-8141(94)90146-5.

Atkinson, B. K., and P. G. Meredith (1987), The theory of subcritical crack growth with application to minerals and rocks, in *Fracture Mechanics of Rock*, edited by B. K. Atkinson, pp. 111–166, Academic, London.

Bernabe, Y., U. Mok, and B. Evans (2006), A note on the oscillating flow method for measuring rock permeability, *Int. J. Rock Mech. Min. Sci.*, *43*, 311–316, doi:10.1016/j.ijrmms.2005.04.013.

Blanpied, M. L., D. A. Lockner, and J. D. Byerlee (1992), An earthquake mechanism based on rapid sealing of faults, *Nature*, *358*, 574–576, doi:10.1038/358574a0.

Brace, W. F. (1965), Some new measurements of linear compressibility of rocks, *J. Geophys. Res.*, *70*, 391–398, doi:10.1029/JZ070i002p00391.

Brace, W. F. (1980), Permeability of crystalline and argillaceous rocks, *Int. J. Rock Mech. Min. Sci*, *17*, 241–251.

Brace, W. F., J. B. Walsh, and W. T. Frangos (1968), Permeability of granite under high pressure, *J. Geophys. Res.*, *73*, 2225–2236, doi:10.1029/JB073i006p02225.

Brantley, S. L., B. Evans, S. H. Hickman, and D. A. Crerar (1990), Healing of microcracks in quartz - Implications for fluid-flow, *Geology*, *18*, 136–139, doi:10.1130/0091-7613(1990)018<0136:HOMIQI>2.3.CO;2.

Brock, W. G., and T. Engelder (1977), Deformation associated with movement of muddy mountain overthrust in Buffington Window, southeastern Nevada, *Geol. Soc. Am. Bull.*, *88*, 1667–1677, doi:10.1130/0016-7606(1977)88<1667:DAWTMO>2.0.CO;2.

Brune, J. N., T. L. Henyey, and R. F. Roy (1969), Heat flow, stress, and rate of slip along the San Andreas Fault, California, *J. Geophys. Res.*, *74*, 3821–3827, doi:10.1029/JB074i015p03821.

Byerlee, J. (1990), Friction, overpressure and fault normal compression, *Geophys. Res. Lett.*, *17*, 2109–2112, doi:10.1029/GL017i012p02109.

Byerlee, J. (1993), Model for episodic flow of high-pressure water in fault zones before earthquakes, *Geology*, *21*, 303–306, doi:10.1130/0091-7613(1993)021<0303:MFEFOH>2.3.CO;2.

Caine, J. S., J. P. Evans, and C. B. Forster (1996), Fault zone architecture and permeability structure, *Geology*, *24*, 1025–1028, doi:10.1130/0091-7613(1996)024<1025:FZAAPS>2.3.CO;2.

Chester, F. M., and J. S. Chester (2000), Stress and deformation along wavy frictional faults, *J. Geophys. Res.*, *105*, 23,421–23,430, doi:10.1029/2000JB900241.

Chester, F. M., and J. M. Logan (1986), Implications for mechanical-properties of brittle faults from observations of the Punchbowl fault zone, California, *Pure Appl. Geophys.*, *124*, 79–106, doi:10.1007/BF00875720.

Cox, S. J. D., and P. G. Meredith (1993), Microcrack formation and material softening in rock measured by monitoring acoustic emissions, *Int. J. Mech. Min. Sci. Geomech. Abstr.*, *30*, 11–24, doi:10.1016/0148-9062(93)90172-A.

Dor, O., T. K. Rockwell, and Y. Ben-Zion (2006), Geological observations of damage asymmetry in the structure of the San Jacinto, San Andreas and Punchbowl faults in Southern California: A possible indicator for preferred rupture propagation direction, *Pure Appl. Geophys.*, *163*, 301–349, doi:10.1007/s00024-005-0023-9.

Dresen, G., and Y. Guéguen (2004), Damage and rock physical properties, in *Mechanics of Fluid Saturated Rocks*, edited by Y. Guéguen and M. Boutéca, pp. 169–217, Elsevier, New York.

Engelder, J. T. (1974), Cataclasis and generation of fault gouge, *Geol. Soc. Am. Bull.*, *85*, 1515–1522, doi:10.1130/0016-7606(1974)85<1515:CAGOF>2.0.CO;2.

Faulkner, D. R., and E. H. Rutter (2000), Comparisons of water and argon permeability in natural clay-bearing fault gouge under high pressure at 20 degrees C, *J. Geophys. Res.*, *105*, 16,415–16,426, doi:10.1029/2000JB900134.

Faulkner, D. R., and E. H. Rutter (2001), Can the maintenance of overpressured fluids in large strike-slip fault zones explain their apparent weakness?, *Geology*, *29*, 503–506, doi:10.1130/0091-7613(2001)029<0503:CTMOOF>2.0.CO;2.

Faulkner, D. R., T. M. Mitchell, D. Healy, and M. J. Heap (2006), Slip on 'weak' faults by the rotation of regional stress in the fracture damage zone, *Nature*, *444*, 922–925, doi:10.1038/nature05353.

Fischer, G. J. (1992), The determination of permeability and storage capacity: Pore pressure oscillation method, in *Fault Mechanics and Transport Properties of Rocks*, edited by B. Evans and T.-F. Wong, pp. 187–212, Academic, London.

Friedman, M. (1963), Petrofabric analysis of experimentally deformed calcite-cemented sandstones, *J. Geol.*, *71*, 12.

González, G. (1990), Patrones estructurales, modelo de ascenso emplazamiento y deformación del Plutón Cerro Cristales, Cordillera de la Costa al Sur de Antofagasta, *Chile, Memoria para optar al título de Geólogo*, Univ. Cat. del Norte, Antofagasta, Chile.

González, G. (1996), Evolución tectónica de la Cordillera de la Costa de Antofagasta (Chile), in *Especial Referencia las Deformaciones Sinmagmáticas del Jurásico Cretácico Inferior, Berl. Geowiss. Abh. Reihe A*, 181, 111 pp.

González, G. (1999), Mechanismo y profundidad de emplazamiento del Plutón Cerro Cristales, Cordillera de la Costa, Antofagasta, Chile, *Rev. Geol. Chile*, *26*, 23.

Haimson, B., and C. Chang (2000), A new true triaxial cell for testing mechanical properties of rock, and its use to determine rock strength and deformability of Westerly granite, *Int. J. Rock Mech. Min. Sci.*, *37*, 285–296, doi:10.1016/S1365-1609(99)00106-9.

Healy, D., R. R. Jones, and R. E. Holdsworth (2006), Three-dimensional brittle shear fracturing by tensile crack interaction, *Nature*, *439*, 64–67, doi:10.1038/nature04346.

Heap, M. J., and D. R. Faulkner (2008), Quantifying the evolution of static elastic properties as crystalline rock approaches failure, *Int. J. Rock Mech. Min. Sci.*, *45*, 564–573, doi:10.1016/j.ijrmms.2007.07.018.

Heiland, J. (2003), Permeability of triaxially compressed sandstone: Influence of deformation and strain-rate on permeability, *Pure Appl. Geophys.*, *160*, 889–908, doi:10.1007/PL00012571.

Henley, R. W. (1984), The geothermal framework of epithermal deposits, in *Geology and Geochemistry of Epithermal Systems*, edited by B. R. Berger and P. M. Bethke, *Soc. Econ. Geol. Rev. Econ. Geol.*, 2, 1–24.

Jaeger, J. C., N. G. Cook, and R. W. Zimmerman(1969), *Fundamentals of Rock Mechanics*, 4th ed., Blackwell, Malden, Mass.

Janssen, C., F. C. Wagner, A. Zang, and G. Dresen (2001), Fracture process zone in granite: A microstructural analysis, *Int. J. Earth Sci.*, *90*, 46–59, doi:10.1007/s005310000157.

Keaney, G. M. J., P. G. Meredith, and S. A. F. Murrell(1998), Laboratory study of permeability evolution in 'tight' sandstone under non-hydrostatic stress conditions, paper presented at Eurock '98, Int. Soc. of Rock Mech. Trondheim, Norway, 8–10 July.

Knipe, R. J. (1992), Faulting processes and fault seal, *Norw. Petrol. Soc. Spec. Publ.*, *1*, 325–342.

Kranz, R. L., J. S. Saltzman, and J. D. Blacic (1990), Hydraulic diffusivity measurements on laboratory rock samples using an oscillating pore pressure method, *Int. J. Rock Mech. Min. Sci.*, *27*, 345–352, doi:10.1016/0148-9062(90)92709-N.

Lachenbruch, A. H., and J. H. Sass (1980), Heat-flow and energetics of the San-Andreas fault zone, *J. Geophys. Res.*, *85*, 6185–6222, doi:10.1029/JB085iB11p06185.

Lavrov, A. (2003), The Kaiser effect in rocks: Principles and stress estimation techniques, *Int. J. Rock Mech. Min. Sci.*, *40*, 151–171, doi:10.1016/S1365-1609(02)00138-7.

Lee, H. S., and T. F. Cho (2002), Hydraulic characteristics of rough fractures in linear flow under normal and shear load, *Rock Mech. Rock Eng.*, *35*, 299–318, doi:10.1007/s00603-002-0028-y.

Lockner, D. A. (1998), A generalized law for brittle deformation of Westerly granite, *J. Geophys. Res.*, *103*, 5107–5123, doi:10.1029/97JB03211.

Lockner, D. A., and J. D. Byerlee (1995), An earthquake instability model based on faults containing high fluid-pressure compartments, *Pure Appl. Geophys.*, *145*, 717–745, doi:10.1007/BF00879597.

Lockner, D. A., J. D. Byerlee, V. Kuksenko, A. Ponomarev, and A. Sidorin (1991), Quasi-static fault growth and shear fracture energy in granite, *Nature*, *350*, 39–42, doi:10.1038/350039a0.

Lockner, D. A., J. D. Byerlee, V. Kuksenko, A. Ponomarev, and A. Sidrin (1992), Observations of quasi-static fault growth from acoustic emissions, in *Fault Mechanics and Transport Properties of Rocks*, edited by B. Evans and T.-F. Wong, pp. 3–31, Academic, San Diego, Calif.

Manning, C. E., and S. E. Ingebritsen (1999), Permeability of the continental crust: Implications of geothermal data and metamorphic systems, *Rev. Geophys.*, *37*, 127–150, doi:10.1029/1998RG900002.

Matthai, S. K., and M. Belayneh (2004), Fluid flow partitioning between fractures and a permeable rock matrix, *Geophys. Res. Lett.*, *31*, L07602, doi:10.1029/2003GL019027.

Miller, S. A., A. Nur, and D. L. Olgaard (1996), Earthquakes as a coupled shear stress high pore pressure dynamical system, *Geophys. Res. Lett.*, *23*, 197–200, doi:10.1029/95GL03178.

Miller, S. A., C. Collettini, L. Chiaraluce, M. Cocco, M. Barchi, and B. J. P. Kaus (2004), Aftershocks driven by a high-pressure CO2 source at depth, *Nature*, *427*, 724–727, doi:10.1038/nature02251.

Moore, D. E., and D. A. Lockner (1995), The role of microcracking in shear-fracture propagation in granite, *J. Struct. Geol.*, *17*, 95–114, doi:10.1016/0191-8141(94)E0018-T.

Morrow, C. A., D. E. Moore, and D. A. Lockner (2001), Permeability reduction in granite under hydrothermal conditions, *J. Geophys. Res.*, *106*, 30,551–30,560, doi:10.1029/2000JB000010.

Nur, A., and J. R. Booker (1972), Aftershocks caused by pore fluid-flow, *Science*, *175*, 885, doi:10.1126/science.175.4024.885.

Paterson, M. S., and T.-F. Wong (2005), *Experimental Rock Deformation: The Brittle Field*, 2nd ed., 348 pp. Springer, Berlin.

Reches, Z., and D. A. Lockner (1994), Nucleation and growth of faults in brittle rocks, *J. Geophys. Res.*, *99*, 18,159–18,173, doi:10.1029/94JB00115.

Rice, J. R. (1992), Fault stress states, pore pressure distributions, and the weakness of the San Andreas Fault, in *Fault Mechanics and Transport Properties in Rocks*, edited by B. Evans and T.-F. Wong, 28 pp., Academic, London.

Rice, J. R., C. G. Sammis, and R. Parsons (2005), Off-fault secondary failure induced by a dynamic slip pulse, *Bull. Seismol. Soc. Am.*, *95*, 109–134, doi:10.1785/0120030166.

Sammonds, P. R., P. G. Meredith, and I. G. Main (1992), Role of pore fluids in the generation of seismic precursors to shear fracture, *Nature*, *359*, 228–230, doi:10.1038/359228a0.

Sanyal, S. K., R. M. Pirnie, G. O. Chen, and S. S. Marsden (1972), Novel liquid permeameter for measuring very low permeability, *SPE J.*, *12*, 206, doi:10.2118/3099-PA.

Scholz, C. H. (1968), Microfracturing and inelastic deformation of rock in compression, *J. Geophys. Res.*, *73*, 1417–1432, doi:10.1029/JB073i004p01417.

Scholz, C. H., N. H. Dawers, J. Z. Yu, and M. H. Anders (1993), Fault growth and fault scaling laws: Preliminary results, *J. Geophys. Res.*, *98*, 21,951–21,961, doi:10.1029/93JB01008.

Shipton, Z. K., J. P. Evans, K. R. Robeson, C. B. Forster, and S. Snelgrove (2002), Structural heterogeneity and permeability in faulted eolian sandstone: Implications for subsurface modeling of faults, *AAPG Bull.*, *86*, 863–883.

Sibson, R. H. (1974), Frictional constraints on thrust, wrench and normal faults, *Nature*, *249*, 542–544, doi:10.1038/249542a0.

Sibson, R. H. (1990), Conditions for fault-valve behaviour, in *Deformation Mechanisms, Rheology and Tectonics*, edited by R. J. Knipe and E. H. Rutter, *Geol. Soc. London Spec. Publ.*, 54, 15–28.

Sibson, R. H. (1994), Crustal stress, faulting, and fluid flow, in *Geofluids: Origin, Migration and Evolution of Fluids in Sedimentary Basins*, edited by J. Parnell, *Geol. Soc. London Spec. Publ.*, 78, 69–84.

Sibson, R. H. (1996), Structural permeability of fluid-driven fault-fracture meshes, *J. Struct. Geol.*, *18*, 1031–1042, doi:10.1016/0191-8141(96)00032-6.

Sleep, N. H. (1995), Ductile creep, compaction, and rate and state-dependent friction within major fault zones, *J. Geophys. Res.*, *100*, 13,065–13,080, doi:10.1029/94JB03340.

Tenthorey, E., C. H. Scholz, E. Aharonov, and A. Leger (1998), Precipitation sealing and diagenesis: 1. Experimental results, *J. Geophys. Res.*, *103*, 23,951–23,967, doi:10.1029/98JB02229.

Townend, J., and M. D. Zoback (2000), How faulting keeps the crust strong, *Geology*, *28*, 399–402, doi:10.1130/0091-7613(2000)28<399:HFKTCS>2.0.CO;2.

Uehara, S., and T. Shimamoto (2004), Gas permeability evolution of cataclasite and fault gouge in triaxial compression and implications for changes in fault-zone permeability structure through the earthquake cycle, *Tectonophysics*, *378*, 183–195, doi:10.1016/j.tecto.2003.09.007.

Uribe, F., and H. Niemeyer (1984), ranjas miloníticas en la Cordillera de la Costa de Antofagasta (Cuadrángulo de Cerro Cristales, 24°00′–24°15′S) y la distribución del basamento precámbrico, *Rev. Geol. Chile*, *23*, 4.

Vermilye, J. M., and C. H. Scholz (1998), The process zone: A microstructural view of fault growth, *J. Geophys. Res.*, *103*, 12,223–12,237, doi:10.1029/98JB00957.

Vidale, J. E., and Y. G. Li (2003), Damage to the shallow Landers fault from the nearby Hector Mine earthquake, *Nature*, *421*, 524–526, doi:10.1038/nature01354.

Wilson, J. E., J. S. Chester, and F. M. Chester (2003), Microfracture analysis of fault growth and wear processes, Punchbowl Fault, San Andreas System, California, *J. Struct. Geol.*, *25*, 1855–1873, doi:10.1016/S0191-8141(03)00036-1.

Zhang, J., W. B. Standifird, J. C. Roegiers, and Y. Zhang (2007), Stress-dependent fluid flow and permeability in fractured media: From lab experiments to engineering applications, *Rock Mech. Rock Eng.*, *40*, 3–21, doi:10.1007/s00603-006-0103-x.

Zhu, W. L., and T. F. Wong (1997), The transition from brittle faulting to cataclastic flow: Permeability evolution, *J. Geophys. Res.*, *102*, 3027–3041, doi:10.1029/96JB03282.

Zhu, W. L., L. G. J. Montesi, and T. F. Wong (1997), Shear-enhanced compaction and permeability reduction: Triaxial extension tests on porous sandstone, *Mech. Mater.*, *25*, 199–214, doi:10.1016/S0167-6636(97)00011-2.

Zoback, M. D., and J. D. Byerlee (1975), Effect of microcrack dilatancy on permeability of Westerly granite, *J. Geophys. Res.*, *80*, 752–755, doi:10.1029/JB080i005p00752.

Zoback, M. D., et al. (1987), New evidence on the state of stress of the San-Andreas Fault system, *Science*, *238*, 1105–1111, doi:10.1126/science.238.4830.1105.

D. R Faulkner, Rock Deformation Laboratory, Department of Earth and Ocean Sciences, University of Liverpool, Liverpool L69 3BX, UK.

T. M. Mitchell, Graduate School of Science, Department of Earth and Planetary Systems Science, Hiroshima, 739-8526, Japan. (tom-mitchell@hiroshima-u.ac.jp)